

HyDRA: A Hybrid Dual-Mode Network for Closed- and Open-Set RFFI with Optimized VMD

Hanwen Liu[#], Yuhe Huang[#], Yifeng Gong[#], Yanjie Zhai[#], Jiaxuan Lu^{*}

Abstract—Device recognition is vital for security in wireless communication systems, particularly for applications like access control. Radio Frequency Fingerprint Identification (RFFI) offers a non-cryptographic solution by exploiting hardware-induced signal distortions. This paper proposes HyDRA, a Hybrid Dual-mode RF Architecture that integrates an optimized Variational Mode Decomposition (VMD) with a novel architecture based on the fusion of Convolutional Neural Networks (CNNs), Transformers, and Mamba components, designed to support both closed-set and open-set classification tasks. The optimized VMD enhances preprocessing efficiency and classification accuracy by fixing center frequencies and using closed-form solutions. HyDRA employs the Transformer Dynamic Sequence Encoder (TDSE) for global dependency modeling and the Mamba Linear Flow Encoder (MLFE) for linear-complexity processing, adapting to varying conditions. Evaluation on public datasets demonstrates state-of-the-art (SOTA) accuracy in closed-set scenarios and robust performance in our proposed open-set classification method, effectively identifying unauthorized devices. Deployed on NVIDIA Jetson Xavier NX, HyDRA achieves millisecond-level inference speed with low power consumption, providing a practical solution for real-time wireless authentication in real-world environments.

Index Terms—Radio frequency fingerprint identification, specific emitter identification, transformer, mamba, VMD, open-set classification

I. INTRODUCTION

Radio Frequency Fingerprint Identification (RFFI) identifies wireless devices by analyzing unique hardware-induced signal distortions caused by manufacturing variations in analog components[1]. These distortions manifest as subtle spectral and temporal signatures, enabling device authentication independent of cryptographic protocols. As wireless networks grow in complexity, RFFI has become indispensable for securing IoT deployments[2][3][4], drone communications[5][6], and mission-critical systems[7][8].

RFFI methodologies are categorized into expert feature-driven approaches and deep learning (DL)-based. Expert methods rely on manually engineered features from time-frequency analysis, such as Hilbert-Huang transforms[9] for transient

distortion characterization, wavelet decompositions[10] for steady-state artifact quantification, local mean decomposition (LMD)[11] for AM/FM signal decomposition and time-varying instantaneous frequency extraction. While interpretable, these approaches suffer from noise sensitivity under low SNR conditions and limited capability to model nonlinear hardware impairment interactions. Their reliance on heuristic feature design further restricts scalability in congested spectral environments[12].

The advent of Deep neural network (DNN) shifted focus toward automated feature extraction[13][14], including Recurrent Neural Network (RNN)[15] and Convolutional Neural Network (CNN)[16][17]. Existing DL-based methods utilize two parallel paradigms: transient and steady-state analysis. Transient-based approaches leverage brief signal transitions to capture hardware fingerprints[18]. However, they require expensive high-speed sampling equipment[19] and degrade severely under mobility-induced Doppler shifts[20]. These limitations are particularly acute in WiFi systems, where rare device reboots result in scarce transient data. In contrast, steady-state methods analyze persistent signal segments like protocol preambles[21][22], which provide deterministic structures unaffected by payload randomness. This enables robust multi-scale periodicity analysis and efficient channel equalization, making steady-state approaches preferable for real-world deployment.

To extract feature of steady-state signal, CNN-based models[23][24] effectively capture hardware-specific features. These models demonstrate strong performance in scenarios with limited devices and short signal segments. However, the inherent limitation of CNNs in modeling global dependencies due to their local receptive fields leads to significant performance degradation when applied to large-scale datasets. To optimize computational efficiency, ADCC[25] employ dilated convolutions and signal truncation preprocessing, reducing computational complexity for edge deployment. However, these optimizations sacrifice time-space resolution, demonstrating that dilated convolutions expand the receptive field but reduce sensitivity to signal variations, while signal truncation may discard device-specific features in later signal segments[26].

Optimized preprocessing methods also contribute on hardware-specific feature and computational efficiency. Zhang et al. [9] utilized energy entropy and Hilbert spectra derived from Empirical Mode Decomposition (EMD)[27] for classification, while Flamant et al. [28] analyzed time-frequency characteristics of bivariate signals. Dragomiretskiy et al. [29] demonstrate that Variational Mode Decomposition (VMD) is adaptive and noise-resistant and can effectively reduce

[#] Contributed equally to this work.

Hanwen Liu and Yifeng Gong are with the School of Electronics and Communication Engineering, Sun Yat-sen University, Shenzhen, 518107, China, e-mail: (liuhw56, gongyf9@mail2.sysu.edu.cn).

Yuhe Huang is with the School of Electronic Information and Electrical Engineering, Shanghai Jiao Tong University, Shanghai, 200240, China, e-mail: yuhehuang@sjtu.edu.cn.

Yanjie Zhai is with the School of Electronic Information and Electrical Engineering, Dalian Maritime University, Dalian, 116026, China, e-mail: yzhai4@outlook.com.

Jiaxuan Lu is with Shanghai Artificial Intelligence Laboratory, Shanghai, 200232, China, e-mail: lujiaxuan@pjlab.org.cn.

^{*} Corresponding Author.

the complexity of time-frequency feature extraction. Despite these advancements, limitations persist: EMD and bivariate characteristics suffer from endpoint effects and frequency aliasing, while the inherent reconstruction artifacts in conventional VMD frameworks progressively compromise spectral fingerprint discernibility through error accumulation in large-scale datasets; additionally, the computational complexity of VMD models imposes significant resource demands, with these limitations escalating exponentially as the number of Intrinsic Mode Functions (IMFs) channels increases.

For the testing method, current research on RFFI predominantly focuses on closed-set testing, where models are trained and evaluated solely on predefined known device categories[30]. However, this approach starkly conflicts with real-world security requirements. In practical wireless communication environments, systems must simultaneously achieve precise identification of authorized devices and effective interception of unauthorized ones. Traditional closed-set models, by forcing all test samples into predefined categories, risk misclassifying unknown devices as legitimate, posing critical security vulnerabilities.

To address these challenges, we propose the HyDRA framework, which integrates lossless Variational Mode Decomposition (VMD) and a reconfigurable dual-encoder architecture to reduce computational time, avoid convergence loss, balance accuracy and efficiency, and enable open-set testing. The architecture dynamically switches between the Transformer Dynamic Sequence Encoder (TDSE) for high-precision tasks and the Mamba Linear Flow Encoder (MLFE) for high-efficiency demands, with the MLFE leveraging a selective state-space model (SSM) to capture long-range dependencies at linear computational complexity. This dual-mode design addresses the diverse requirements of real-world wireless communication systems, where high-precision identification is critical in secure, high-stakes environments, while rapid, energy-efficient processing is essential for resource-constrained edge devices. Channel-aware feature fusion is enhanced through split-path residual blocks that decouple magnitude and phase processing in the RF domain, using adaptive concatenation weights adjusted by a Convolutional Feature Refinement Extractor (CFRE) to extract multi-scale temporal features. We further redesign VMD by fixing central frequencies and deriving closed-form expressions for Intrinsic Mode Function (IMF) components, eliminating the iterative Alternating Direction Method of Multipliers (ADMM) to minimize computational time and reconstruction losses. For open-set testing, we introduce a threshold discrimination-based classification framework that utilizes the model's softmax probability distribution to assess device identity reliability, flagging devices as unauthorized if the highest probability falls below a preset threshold, thereby enhancing robustness in real-world scenarios. Our contributions are:

- We propose the HyDRA dual-mode framework, integrating optimized lossless VMD with a CNN-Transformer-Mamba network, achieving SOTA accuracy in closed-set testing on the WiSig dataset[31] and pioneering open-set testing.
- We introduce a dynamic dual-encoder architecture: TDSE

enabling global modeling under high SNR conditions, MLFE using selective state space models for linear complexity, achieving millisecond-level speed with low power consumption on NVIDIA Jetson Xavier NX.

- A data processing method is developed by fixing VMD central frequencies and using closed-form solutions to eliminate ADMM reconstruction error. This method achieves higher accuracy on the WiSig dataset[31] compared to raw IQ data and VMD (ADMM), while significantly reducing decomposition time compared to VMD (ADMM).
- A threshold discrimination-based open-set classification mechanism is proposed, achieving a peak accuracy of 94.67% in detecting illegal devices during open-set testing, enhancing RFFI robustness in real-world scenarios.

II. RELATED WORKS

A. Spectral Feature-Based RFFI

Early works established foundational techniques for hardware fingerprint extraction through time-frequency analysis. Zhang et al. [9] pioneered Hilbert-Huang transforms to characterize transient signal distortions, while Dragomiretskiy et al. [29] introduced VMD to decompose signals into narrow-band IMFs. Subsequent studies explored dual-tree wavelet transforms [10] for multi-resolution analysis and I/Q imbalance metrics [32] for steady-state feature extraction. These methods achieved promising results in controlled scenarios but faced limitations in dynamic environments due to fixed decomposition parameters, which restricted their adaptability to channel variations and hardware diversity. Rehman et al. [12] proposed utilizing the spectrogram of a short-time Fourier transform to obtain the energy envelope of instantaneous transient signals and extract unique features from the envelope for validation through Bluetooth signal recognition. Recent advancements by Liang et al. [33] developed adaptive VMD through reinforcement learning, dynamically adjusting decomposition parameters based on channel state information. Han et al. [34] integrated VMD with Transformer encoders, achieving 67.83% recognition accuracy under mobility conditions—a critical step toward adaptive decomposition frameworks.

B. Deep Learning-Based RFFI

Deep learning paradigms revolutionized RFFI through automated feature learning. Transient analysis leverages temporal dynamics of signal activation states. For example, CNNs [16] achieved 93% accuracy in classifying ZigBee power-on signatures by capturing abrupt waveform transitions, while recurrent networks [35] modeled sequential dependencies in transient phases. Steady-state methods prioritize computational efficiency and hardware compatibility. Merchant et al. [2] demonstrated the viability of CNN-based WiFi preamble analysis, attaining 89% accuracy with 25 Msps sampling rates, thereby balancing precision and resource constraints. Hybrid architectures synergize domain knowledge with adaptive learning. Transformers [7] leveraged self-attention for long-range dependency modeling, achieving 91% accuracy on IEEE 802.11a/g signals. Hybrid frameworks further bridged transient

and steady-state paradigms; Han et al. [34] proposed a VMD-Transformer architecture that decomposes ADS-B signals into multi-frequency IMFs and leverages multi-head self-attention to jointly model high-to-low frequency components. This approach effectively captures both transient spectral distortions and steady-state periodic features, achieving 67.83% recognition accuracy under mobility-induced Doppler shifts and multipath interference—demonstrating significant robustness in real-world UAV identification tasks. These works collectively validated the integration of signal processing priors with adaptive neural architectures, paving the way for dynamic reconfigurable systems.

III. METHOD

This section presents HyDRA, a dual-mode framework for radio frequency fingerprinting (RFF) to identify transmitters using IQ data. HyDRA integrates optimized lossless VMD, a dual-mode neural network with Transformer or Mamba encoding, Classifier for either closed- or open-set classification. The framework is illustrated in Figure 1.

A. Variational Mode Decomposition

Variational Mode Decomposition (VMD) is an algorithm proposed by Dragomiretskiy et al. [29] in 2014, aiming at decomposing a signal into Intrinsic Mode Function (IMF) components, while ensuring that each component has limited bandwidth. Han et al. [34] have utilized VMD in RFFI and proved that its performance overcomes other mode decomposition methods such as EMD and LMD.

The constrained variational problem of VMD can be expressed as

$$\arg \min_{\{u_k\}, \{\omega_k\}} \left\{ \sum_k \left\| \partial_t \left[\left(\delta(t) + \frac{j}{\pi t} \right) * u_k(t) \right] e^{-j\omega_k t} \right\|_2^2 \right\} \quad (1)$$

$$s.t. \sum_k u_k(t) = f(t)$$

where $f(t)$ is the input signal, k is the number of modes, $u_k(t)$ is the time-domain expression of the k -th mode, and $\omega_k(t)$ is the center frequency of the k -th mode. ∂_t is the derivative w.r.t. t , $*$ denotes the convolution in signal processing and $\|\cdot\|_2$ denotes the L^2 norm in functional space $C(-\infty, \infty)$.

By expanding the L^2 norm and applying the Parseval's theorem (See Appendix A), the problem can be analyzed in frequency domain, that is

$$\arg \min_{\{U_k\}, \{\omega_k\}} \left\{ \sum_k \int_0^\infty 4(\omega - \omega_k)^2 |U_k(\omega)|^2 d\omega \right\} \quad (2)$$

$$s.t. \sum_k U_k(\omega) = F(\omega)$$

where $U_k(\omega)$ and $F(\omega)$ are the Fourier transform of $u_k(t)$ and $f(t)$, respectively. Evidently, the loss function limits the bandwidth of each mode by penalizing its frequency components far away from its central frequency.

Dragomiretskiy et al. [29] introduced an ADMM (Alternate Direction Method of Multipliers) algorithm to solve the optimization problem eq. (2). However, this method introduced

significant reconstruction error due to relevant terms in the augmented Lagrangian (See Figure 2). This error may serve as denoising at low SNR, but at high SNR, it could be unfavorable for RFFI because it may filter out the crucial spectral features of the transmitter. Furthermore, Figure 2 shows that in certain circumstances, the algorithm would locate the central frequencies wrongly. As a result, a spectral peak would be strongly suppressed.

To deal with the drawbacks of ADMM algorithm, we proposed an optimized algorithm based on the closed-form solution of eq. (2), shown in eq. (3). (For mathematical details, see Appendix A).

$$U_k(\omega) = F(\omega) \cdot \frac{(\omega - \omega_k)^{-2}}{\sum_i (\omega - \omega_i)^{-2}} \quad (3)$$

The center frequencies ω_k can be determined by solving the optimization problem eq. (4).

$$\arg \min_{\{\omega_k\}} \int_0^\infty \frac{|F(\omega)|^2}{\sum_k (\omega - \omega_i)^{-2}} d\omega \quad (4)$$

In practice, the spectrum of a digitally modulated signal reaches a peak at multiples of its fundamental frequency $2\pi/T_s$, where T_s denotes the symbol duration. To suppress the penalty term, the central frequencies of the modes $\{\omega_k\}$ can be directly assigned as multiples of $2\pi/T_s$, without having to solve the optimization problem eq. (4). This approach is more robust, since the central frequencies are manually assigned, eliminating the possibility of location error. In the rest of the paper, this method will be named as **lossless VMD**, since it does not introduce information loss during decomposition.

To process discrete signals, we transform eq. (3) into its discrete version eq. (5).

$$U_i(k) = F(k) \cdot \frac{(k - k_i)^{-2}}{\sum_j (k - k_j)^{-2}}, \quad k = 0, 1, \dots, L-1 \quad (5)$$

where k_i is the corresponding DFT index of the i -th central frequency.

With the sampling rate and symbol rate of the dataset known, we can calculate the corresponding DFT index k_0 of the fundamental frequency $2\pi/T_s$. As we have discussed, each selected central frequency should be a multiple of k_0 .

$$k_0 = \frac{f_{sample}}{f_{symbol}} \quad (6)$$

VMD can serve as data enhancement by splitting each input into k channels. In our model, the VMD preprocessing layer is a transformation $\phi : \mathbb{R}^{L \times 2} \rightarrow \mathbb{R}^{L \times k \times 2}$, mapping the IQ input into VMD-decomposed data.

B. Hybrid Dual-Mode Network Design

The HyDRA (TDSE/MLFE) is designed for radio frequency fingerprint identification, integrating multiple components to process the input signal and produce the final classification output. Specifically, it comprises the Convolutional Feature Refinement Extractor (CFRE), a dual-mode encoder implemented as either the Transformer Dynamic Sequence Encoder (TDSE) or the Mamba Linear Flow Encoder (MLFE), and the

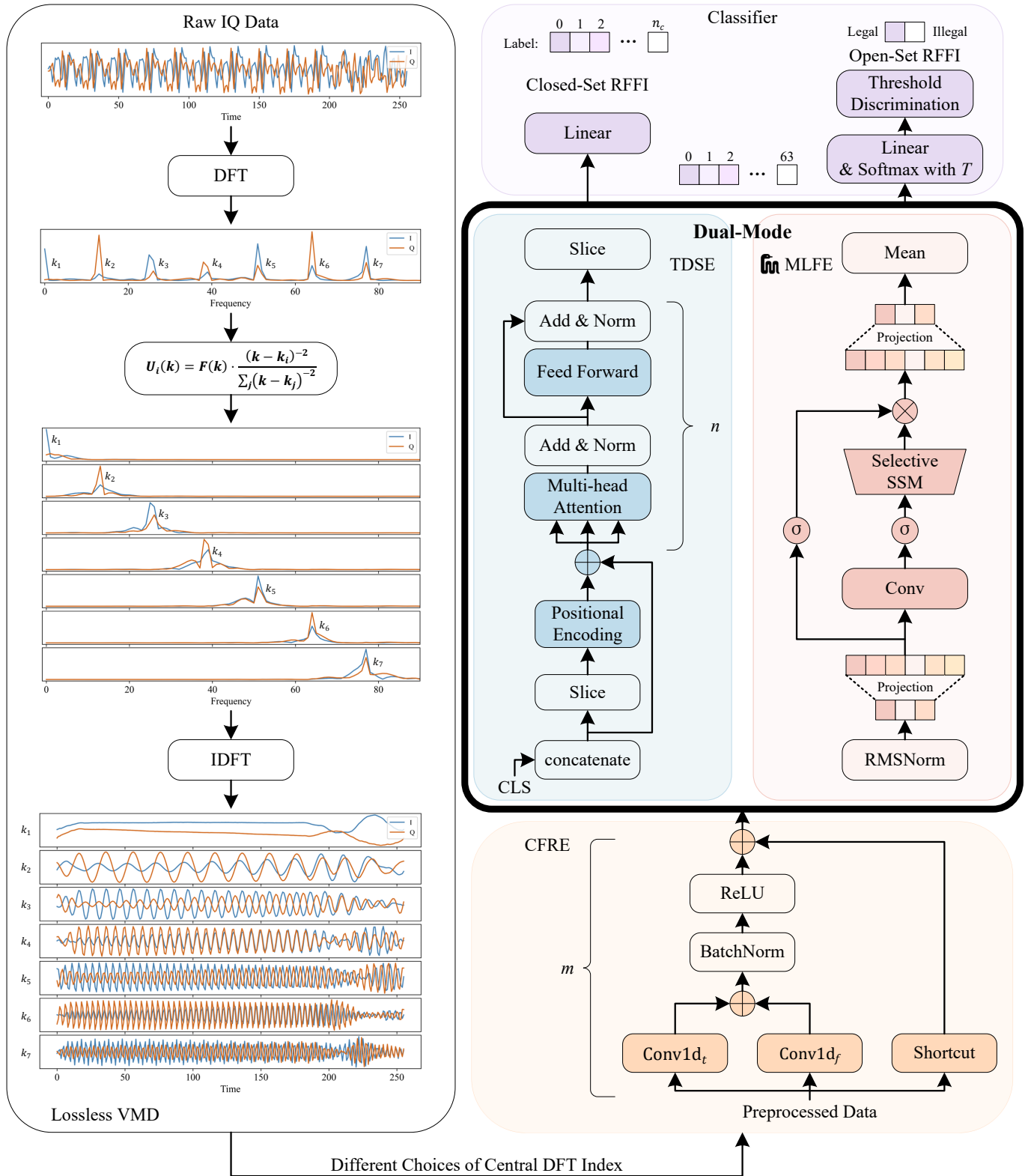


Fig. 1: The framework of HyDRA. Input IQ data is processed via lossless VMD, selecting central DFT frequencies as preprocessed data. These are refined by the Convolutional Feature Refinement Extractor (CFRE), encoded by a dual-mode encoder—either the high-precision Transformer Dynamic Sequence Encoder (TDSE) or the efficient Mamba Linear Flow Encoder (MLFE)—and processed through either the Closed-Set RFFI for known RF fingerprint identification or the Open-Set RFFI for detecting unknown transmitters.

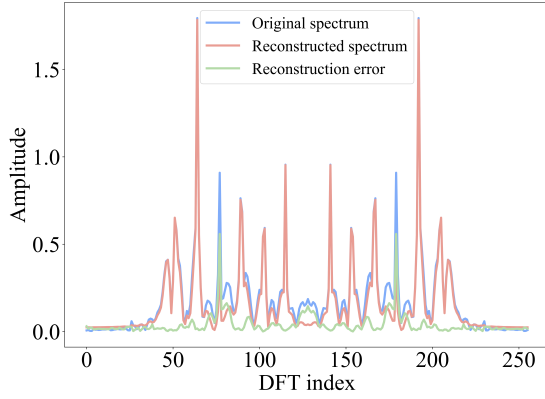


Fig. 2: Reconstruction Error of ADMM (k=6).

Classifier (including Closed- and Open-Set RFFI). The dual-mode encoder processes X_{feat} , offering two configurations: a TDSE mode for high precision and an MLFE mode for efficiency. The overall process is mathematically expressed as:

$$X_{\text{feat}} = \text{CFRE}(X), \quad (7)$$

$$X_{\text{enc}} = \text{Encoder}(X_{\text{feat}}), \quad (8)$$

$$\hat{Y} = \text{Classifier}(X_{\text{enc}}), \quad (9)$$

where $X \in \mathbb{R}^{b \times T \times c}$ is the input tensor, $X_{\text{feat}} \in \mathbb{R}^{b \times T \times d_m}$ is the feature representation, X_{enc} is the encoded sequence (with shape $\mathbb{R}^{b \times (T+1) \times d_m}$ for TDSE and $\mathbb{R}^{b \times T \times d_m}$ for MLFE), and $\hat{Y} \in \mathbb{R}^{b \times n_c}$ is the predicted output, with b as the batch size, T as the sequence length, c as the input channels, d_m as the feature dimension, and n_c as the number of classes. Weights for convolutional and linear layers are initialized with $\mathcal{N}(0, 0.02)$, and batch normalization parameters are initialized with weights of 1 and biases of 0. The following subsections detail each component.

1) Convolutional Feature Refinement Extractor (CFRE):

The CFRE module extracts robust features from the input tensor $X \in \mathbb{R}^{b \times T \times c}$, where c represents the number of input channels. For IQ data, $c = 2$ (in-phase and quadrature components), while for VMD data, $c = 2k$ (number of variational mode decomposition components). The input is permuted to $\mathbb{R}^{b \times c \times T}$ for 1D convolution along the temporal dimension. The ResConv1d block, a residual convolutional layer, combines multi-scale temporal features. For an input $X_{\text{in}} \in \mathbb{R}^{b \times c_{\text{in}} \times T}$, it applies a shortcut path using a 1x1 convolution if the input and output channel dimensions differ or an identity mapping otherwise, followed by two convolutional operations: one with kernel size k_t and dilation d with padding $p_t = \lfloor k_t/2 \rfloor \cdot d$, and another with a larger kernel size k_f and padding p_f . The forward pass is:

$$X_{\text{id}} = \text{Shortcut}(X_{\text{in}}), \quad (10)$$

$$X_t = \text{Conv1d}_t(X_{\text{in}}), \quad (11)$$

$$X_f = \text{Conv1d}_f(X_{\text{in}}), \quad (12)$$

$$X_{\text{out}} = \text{ReLU}(\text{BN}(X_t + X_f)) + X_{\text{id}}, \quad (13)$$

where X_{id} is the shortcut output, X_t and X_f are the temporal feature maps, and $X_{\text{out}} \in \mathbb{R}^{b \times c_{\text{out}} \times T}$ is the block output. The extractor uses a unified pathway with three ResConv1d layers transforming channels sequentially with increased dilation in the intermediate layer, yielding $X_{\text{feat}} \in \mathbb{R}^{b \times T \times d_m}$.

2) *Transformer Dynamic Sequence Encoder (TDSE)*: In TDSE mode, implemented as Trans-FluxEncoder, a learnable positional encoding is applied, initialized as a tensor $P \in \mathbb{R}^{1 \times T_{\text{max}} \times d_m}$ with $\mathcal{N}(0, 0.02)$, where T_{max} is the maximum sequence length. The encoding is trimmed and added to the input:

$$X_{\text{pos}} = X_{\text{feat}} + P[:, : T, :], \quad (14)$$

where $P[:, : T, :] \in \mathbb{R}^{1 \times T \times d_m}$ adapts to the input length, enabling the model to learn position-specific patterns. A classification token $X_c \in \mathbb{R}^{1 \times 1 \times d_m}$, initialized with $\mathcal{N}(0, 0.02)$, is expanded to $\mathbb{R}^{b \times 1 \times d_m}$ and concatenated, forming $X_{\text{seq}} \in \mathbb{R}^{b \times (T+1) \times d_m}$. The sequence is processed by L layers of a Transformer encoder, each with H attention heads, feedforward dimension d_f , and dropout δ , using GELU activation. The multi-head self-attention mechanism, a cornerstone of the Transformer, computes attention for head h as:

$$\Lambda_h = \text{softmax} \left(\frac{Q_h K_h^\top}{\sqrt{d_k}} \right) V_h, \quad (15)$$

where $Q_h = X_{\text{seq}} W_h^Q$, $K_h = X_{\text{seq}} W_h^K$, $V_h = X_{\text{seq}} W_h^V$ are the query, key, and value projections, with $W_h^Q, W_h^K, W_h^V \in \mathbb{R}^{d_m \times d_k}$, and $d_k = d_m/H$ is the per-head dimension. The outputs are concatenated and transformed:

$$\text{MultiHead}(X_{\text{seq}}) = \text{Concat}(\Lambda_1, \dots, \Lambda_H) W^O, \quad (16)$$

where $W^O \in \mathbb{R}^{d_m \times d_m}$ is the output projection. Each layer combines attention with a feedforward network and residual connections, yielding $X_{\text{enc}} \in \mathbb{R}^{b \times (T+1) \times d_m}$, capturing global dependencies with quadratic complexity in T . The classification token embedding is then extracted as $X_{\text{co}} = X_{\text{enc}}[:, 0, :] \in \mathbb{R}^{b \times d_m}$ for subsequent prediction.

3) *Mamba Linear Flow Encoder (MLFE)*: In MLFE mode, implemented as Mamba-StreamEncoder, X_{feat} is processed by a single Mamba layer, leveraging a selective state-space model (SSM) for linear complexity. The SSM reinterprets sequence modeling as a continuous system, using input-dependent parameters to efficiently capture long-range dependencies. The dynamics for each step $t = 1, \dots, T$ are defined as:

$$h_t = \bar{A}h_{t-1} + \bar{B}x_t, \quad (17)$$

$$y_t = Ch_t, \quad (18)$$

where $x_t \in \mathbb{R}^{b \times d_m}$ is the input at time t , $h_t \in \mathbb{R}^{b \times d_s}$ is the hidden state, $y_t \in \mathbb{R}^{b \times d_m}$ is the output, and d_s is the state dimension. The parameters $\bar{A} \in \mathbb{R}^{b \times d_s \times d_s}$, $\bar{B} \in \mathbb{R}^{b \times d_s \times d_m}$, and $C \in \mathbb{R}^{b \times d_m \times d_s}$ are input-dependent, generated via a linear projection of x_t to produce Δ, B, C , where $\Delta \in \mathbb{R}^{b \times T \times d_m}$ is a timescale parameter (softplus-activated), and discretization yields $\bar{A} = \exp(\Delta \cdot A)$ and $\bar{B} = \Delta \cdot B$, with $A \in \mathbb{R}^{d_s \times d_s}$ as a learnable base matrix. The input is expanded by a factor e , processed with a 1D convolution of kernel size k_c , and selectively gated with SiLU activation, producing

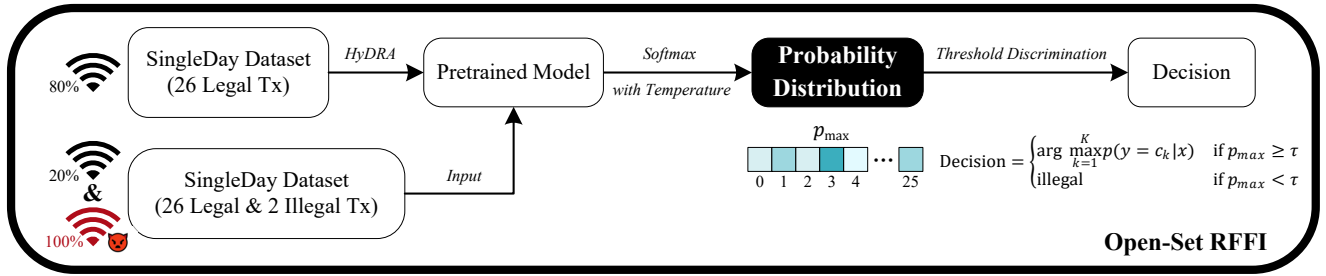


Fig. 3: The Open-Set RFFI framework employs the HyDRA (TDSE) model, trained on 80% of the SingleDay dataset’s 26 legal transmitters (Tx), with the remaining 20% and 100% of 2 illegal Tx used for testing. This split balances the proportion of legal and illegal data. The pretrained model outputs a softmax probability distribution over known classes, followed by threshold discrimination to classify device legitimacy.

$X_{\text{enc}} \in \mathbb{R}^{b \times T \times d_m}$. This design efficiently captures long-range dependencies, contrasting with the TDSE’s attention-based approach. The sequence is then mean-pooled over time as $X_{\text{co}} = X_{\text{enc}}.\text{mean}(\text{dim} = 1) \in \mathbb{R}^{b \times d_m}$ for subsequent prediction.

4) *Closed-Set RFFI*: The Closed-Set RFFI generates predictions from X_{co} . The output is:

$$\hat{Y} = X_{\text{co}}W + b \in \mathbb{R}^{b \times n_c}, \quad (19)$$

where $W \in \mathbb{R}^{d_m \times n_c}$ and $b \in \mathbb{R}^{n_c}$ are learnable parameters, and n_c is the number of classes.

C. Open-Set RFFI

Current DL-based radio frequency fingerprinting systems predominantly rely on closed-set classification, where models are trained and tested on fixed datasets containing only known devices. In this paradigm, the classifier assumes that all test samples belong to one of the classes observed during training, i.e., $C = \{c_1, c_2, \dots, c_K\}$, where K is the number of known classes. While effective in controlled environments, this approach fails in real-world security applications when unfamiliar or unauthorized devices transmit data. As noted by Al-Hazbi et al. [36], most existing DL-based RFF systems struggle with new, unseen devices because they have not encountered their unique RF fingerprints during training, leading to unreliable recognition and misclassification based on the closest match from the training set. This limitation underscores the need for open-set classification techniques to enhance system security and adaptability in dynamic, real-world scenarios.

To enhance the security of RFF systems and address the limitations of traditional classification, we developed an algorithm based on open-set classification principles. Unlike closed-set classification, open-set classification accounts for test samples that may belong to unknown classes $C_{\text{unknown}} \not\subset C$, not seen during training. The algorithm has two primary objectives: (1) accurately classify samples from known classes C as legal, and (2) identify samples from unknown classes as illegal. This distinction between legal and illegal transmitters strengthens the security of RFF systems for real-world applications. Our approach, depicted in Figure 3, leverages the probability distribution from the model’s final softmax layer, incorporating a temperature parameter to control the smoothness

of the output distribution. For a given input sample x , the softmax layer generates a probability distribution over the known classes, denoted as $p(y = c_k|x)$ for $k = 1, 2, \dots, K$, where $\sum_{k=1}^K p(y = c_k|x) = 1$. The softmax function with temperature is defined as:

$$p(y = c_k|x) = \frac{e^{z_k/T}}{\sum_{j=1}^K e^{z_j/T}} \quad (20)$$

where z_k is the raw score (logit) for class c_k , T is the temperature parameter, K is the number of known classes, and $p(y = c_k|x)$ represents the predicted probability of the input x belonging to class c_k . The temperature parameter T controls the smoothness of the probability distribution: a higher T produces a softer, more uniform distribution, while a lower T sharpens the probabilities, approaching the standard softmax behavior when $T = 1$. In a well-trained model, the softmax output for a sample from a known device typically assigns a high probability—often close to 1—to the correct class. For an unknown device, the probabilities are generally lower and more evenly distributed across classes, and the temperature parameter enhances the model’s ability to distinguish these cases by adjusting the confidence of the predictions.

We introduce a threshold discrimination mechanism based on the maximum softmax probability, defined as:

$$p_{\text{max}} = \max_{k=1}^K p(y = c_k|x) \quad (21)$$

The classification decision is formalized as follows:

$$\text{Decision} = \begin{cases} \arg \max_{k=1}^K p(y = c_k|x) & \text{if } p_{\text{max}} \geq \tau \\ \text{illegal} & \text{if } p_{\text{max}} < \tau \end{cases} \quad (22)$$

Here, τ is a predefined threshold. If $p_{\text{max}} \geq \tau$, the sample is classified as belonging to the specific known class given by $\arg \max_{k=1}^K p(y = c_k|x)$, indicating it likely originates from a recognized device associated with that class. Conversely, if $p_{\text{max}} < \tau$, the sample is classified as illegal, suggesting it comes from an unknown or unauthorized device. The threshold τ serves as a confidence boundary in this threshold discrimination process, separating samples the model recognizes with sufficient certainty for a specific known class from those it does not.

TABLE I
THE ACCURACIES AND F1 SCORES OF DIFFERENT METHODS ON SINGLEDAY AND MANYTX DATASETS. BEST RESULTS IN **BOLD**.

Dataset	Preprocessing	HyDRA (TDSE)		HyDRA (MLFE)	
		ACC (%)	F1 (%)	ACC (%)	F1 (%)
SingleDay	None	99.78	99.78	99.67	99.67
	VMD (ADMM), k=3	99.60	99.59	99.51	99.51
	lossless VMD, k=3	99.81	99.81	99.71	99.71
ManyTx	None	90.22	92.05	89.34	90.09
	VMD (ADMM), k=3	89.46	91.62	86.04	87.57
	lossless VMD, k=3	90.71	92.47	89.82	91.32

TABLE II
DATASET INFORMATION

Dataset	Tx No.	Length	Format	Entries	Entries/Tx
SingleDay	28	256	IQ	224000	8000
ManyTx	150	256	IQ	511515	1556-3600

IV. EXPERIMENT SETUP

A. Dataset

In our experimental setup, we utilize two pre-packaged subsets from the WiSig dataset [31], a large-scale WiFi signal collection designed for receiver and channel-agnostic RF fingerprinting. The SingleDay subset contains 28 transmitters (Tx) and 10 receivers (Rx) captured over a single day, with each Tx-Rx pair providing 800 IEEE 802.11a/g preamble signals at 2 Msps symbol rate (1.0 GB total). The ManyTx subset spans four capture days and includes 150 Tx and 18 Rx, with each Tx-Rx-day combination containing at least 50 signals (2.5 GB total), while tolerating a 10% imbalance in per-receiver signal counts. Both subsets use equalized preamble signals processed through MMSE channel equalization to mitigate wireless channel effects. We selected these subsets to address distinct experimental requirements: SingleDay facilitates controlled analysis of receiver-specific variations under consistent channel conditions, while ManyTx enables large-scale transmitter discrimination across multiple days and receivers. The dataset’s preprocessing ensures compatibility with deep learning workflows by providing standardized 256-sample IQ sequences sampled at 25 Msps. Our choice aligns with the dataset authors’ recommendations for benchmarking generalization across hardware and temporal variations. Table II concludes the essential information for model training of the two datasets.

B. Baseline Methods

This study evaluates the effectiveness of our proposed HyDRA model for Radio Frequency Fingerprinting by benchmarking it against a suite of recognized baseline approaches. These methods, spanning convolutional, contrastive, and transformer-based architectures, are detailed below, providing a comprehensive comparison to assess HyDRA’s performance.

1) CNN (CNN-based)[37]: This conventional CNN baseline processes raw IQ samples through stacked convolutional layers

TABLE III
IDENTIFICATION RESULTS OF DIFFERENT METHODS ON THE MANYTX AND SINGLEDAY DATASETS. BOTH DATASETS HAVE NOT BEEN PREPROCESSED. THE BEST RESULTS ARE HIGHLIGHTED IN **BOLD**.

Dataset	Method	ACC (%)
SingleDay	CNN[37]	85
	CNN-TFLite[38]	99
	Transformer-ResNet[39]	93
	Transformer-TFLite[38]	98
	HyDRA(TDSE)	99.78
	HyDRA(MLFE)	99.67
ManyTx	WiSigNet[31]	53.1
	WiSigNet MCRFF[40]	71.6
	MobileNet[41]	84.5
	MobileNet MCRFF[40]	86.4
	HyDRA(TDSE)	90.22
HyDRA(MLFE)	89.34	

* All model results used for comparison are sourced from the cited paper.

and pooling operations to extract hierarchical spatial and temporal features from RF signals. It uses convolutional kernels to capture patterns in IQ data and fully connected layers for device classification, focusing on the real and imaginary components to identify unique transmitter characteristics.

2) CNN-TFLite (CNN-based)[38]: This CNN is optimized for edge deployment using TensorFlow Lite (TFLite). It features a streamlined architecture with quantization to reduce model size and latency, targeting real-time RFF on resource-limited devices.

3) Transformer-ResNet (Transformer-based)[39]: This hybrid architecture combines Transformers’ contextual learning with ResNet’s robust feature extraction. It processes IQ samples using the Transformer’s multi-head attention to model long-range dependencies and temporal relationships, while ResNet blocks extract deep, discriminative features, capturing complex, multi-scale RF signal patterns for effective device classification.

4) Transformer-TFLite (Transformer-based)[38]: This method adapts a Transformer encoder for edge use with TFLite optimization. It employs a multi-head self-attention mechanism to analyze IQ samples, focusing on capturing intricate signal relationships in a lightweight format.

5) WiSigNet (CNN-based)[31]: WiSigNet, the original convolutional neural network (CNN) proposed by the WiSig dataset authors (denoted as WiSigNet for clarity), is a con-

volutional neural network (CNN) designed to extract features from raw IQ samples. It relies on a traditional CNN structure to capture spatial patterns in radio frequency signals for device identification.

6) WiSigNet MCRFF (CNN-based)[40]: An enhanced version of WiSigNet, WiSigNet MCRFF integrates the meta-contrastive learning framework from MCRFF. It enhances feature extraction by optimizing the similarity between representations of seen and unseen devices, leveraging contrastive loss to improve discriminability.

7) MobileNet (CNN-based)[41]: Built on the MobileNetV2 architecture, this lightweight CNN prioritizes computational efficiency. It employs depthwise separable convolutions to process IQ samples, making it suitable for resource-constrained environments while extracting spatial features.

8) MobileNet MCRFF (CNN-based)[40]: This method integrates MobileNet with the MCRFF framework. By applying meta-contrastive learning, it refines feature extraction to enhance generalization across devices, combining MobileNet’s efficiency with advanced training techniques.

C. Training and Testing Strategies for Closed- and Open-Set RFFI

This subsection outlines the training and testing strategies for closed-set and open-set Radio Frequency Fingerprint Identification (RFFI) using the HyDRA framework. Each dataset is stratified into three subsets: 80% for training (D_{train}) to optimize model parameters, 10% for validation (D_{val}) to tune hyperparameters and enable early stopping, and 10% for testing (D_{test}) to assess final performance. Stratification preserves class distributions across partitions, maintaining balance in imbalanced scenarios. A deterministic shuffling algorithm with a fixed random seed (42) ensures consistent splits across trials. A ReduceLROnPlateau scheduler adjusts the learning rate when validation loss plateaus, stabilizing training.

For closed-set RFFI, we train and evaluate the model to classify known transmitters using both the SingleDay and ManyTx datasets. These datasets are split as described above, with all samples from known classes used across training, validation, and test sets. This approach assesses the model’s accuracy in identifying registered transmitters within a predefined class set, suitable for controlled environments.

For open-set RFFI, we select the HyDRA (TDSE) model for high accuracy and randomly divide the SingleDay dataset’s 28 transmitters into 26 legal and 2 illegal ones to balance sample sizes. We train and validate the model using only the 26 legal transmitters, following the same 8:1:1 split as closed-set testing, while closed-set testing includes all 28 transmitters. The open-set test set (D_{test}) includes test samples from the 26 legal transmitters plus all data from the 2 illegal transmitters, simulating a real-world scenario where unauthorized devices must be detected. This setup, illustrated in Figure 3, enables the model to classify legal transmitters into their correct classes while identifying illegal ones as unauthorized. Using the SingleDay dataset ensures data consistency, as all samples are collected on the same day, reflecting realistic operational conditions. Additionally, this approach balances legal and

TABLE IV
CHOICE OF CENTRAL DFT INDEX

Mode Number k	Central DFT index k_i
2	$\{2k_0, 4k_0\}$
3	$\{k_0, 3k_0, 5k_0\}$
4	$\{0, 2k_0, 4k_0, 6k_0\}$
5	$\{0, k_0, 3k_0, 5k_0, 6k_0\}$
6	$\{k_0, 2k_0, 3k_0, 4k_0, 5k_0, 6k_0\}$
7	$\{0, k_0, 2k_0, 3k_0, 4k_0, 5k_0, 6k_0\}$

illegal samples with a ratio of approximately 13:10, ensuring a fair evaluation.

In the open-set approach, the model outputs the highest probability across known classes, defined as $p_{\text{max}} = \max_k p(y = c_k|x)$. A threshold τ determines classification outcomes:

- A legal sample is correctly classified if $p_{\text{max}} \geq \tau$, assigned to the class $\arg \max_{k=1}^K p(y = c_k|x)$.
- An illegal sample is correctly classified if $p_{\text{max}} < \tau$.

Formally, with N total test samples (N_{legal} legal and N_{illegal} illegal), accuracy is computed as:

$$\text{Accuracy} = \frac{N_{\text{correct, legal}} + N_{\text{correct, illegal}}}{N} \quad (23)$$

where $N_{\text{correct, legal}}$ represents legal samples correctly classified into their classes with $p_{\text{max}} \geq \tau$, and $N_{\text{correct, illegal}}$ denotes illegal samples rejected with $p_{\text{max}} < \tau$. This threshold-based mechanism leverages softmax probabilities to enable robust open-set classification, accurately distinguishing known from unknown transmitters in realistic RFFI applications.

D. Parameter Settings

The central frequencies of the lossless VMD layer w.r.t k for the proposed HyDRA are summarized in Table IV. From the spectrum of the signals in the dataset, we observe that the last peak appears at DFT index near $6k_0 = 75$. For each mode number k , we want to choose the central frequencies as uniformly distributed as possible on the k -axis, while maintaining each one as a multiple of k_0 . Here the sample and symbol rate of the dataset are $f_{\text{sample}} = 25$ Msps and $f_{\text{symbol}} = 2$ Msps, respectively, resulting in $k_0 = 12.5$.

Training parameters for the proposed HyDRA are summarized in Table V. Model training employs the cross-entropy loss function with class weights to address potential imbalances, optimized using the Adam optimizer with an initial learning rate of 1×10^{-3} . A ReduceLROnPlateau scheduler adjusts the learning rate by a factor of 0.1 when validation loss plateaus over 10 epochs, with a minimum learning rate threshold of 1×10^{-5} triggering early stopping. The batch size is fixed at 32 across all datasets, and training extends up to a maximum of 1000 epochs, with the model achieving the lowest validation loss selected for test evaluation.

Model parameters for the proposed HyDRA, operating in Transformer (TDSE) and Mamba (MLFE) modes, are given in Table VI. The number of encoding layers varies by mode: L_{TDSE} is set to 2 for the TDSE to provide sufficient depth for sequential processing, while L_{MLFE} is set to 1 for the

TABLE V
TRAINING PARAMETERS

Parameter	Meaning	Value
optimizer		Adam
lr	initial learning rate	1×10^{-3}
scheduler		ReduceLRonPlateau
γ	factor of lr reduction	0.1
patience	patience to trigger lr reduction	10
lr_{min}	minimal learning rate	1×10^{-5}
batch size		32
max epochs	maximum training epochs	1000

TABLE VI
MODEL PARAMETERS

Parameter	Meaning	Value
L_{TDSE}	Number of TDSE layers	2
L_{MLFE}	Number of MLFE layers	1
k_t	Temporal convolutional kernel size	3
k_f	Fixed convolutional kernel size	15
d_m	Feature dimension	64
H	Number of attention heads (TDSE)	4
d_f	Feedforward dimension (TDSE)	128
d_s	State dimension (MLFE)	16
k_c	Convolutional kernel size (MLFE)	4
e	Expansion factor (MLFE)	2

MLFE to optimize computational efficiency. The convolutional kernel size in the ResConv1d block is set to $k_t = 3$ for one convolutional path and $k_f = 15$ for the other, enabling the capture of both localized and broader temporal patterns in the input data. The feature dimension d_m is configured at 64, balancing representational capacity and computational efficiency. For the TDSE mode, the number of attention heads H is set to 4, and the feedforward dimension d_f is 128, optimizing multi-head attention dynamics. In the MLFE mode, the state dimension d_s of the selective state-space model (SSM) is fixed at 16, the convolutional kernel size k_c is 4, and the expansion factor e is 2, enhancing the SSM’s efficiency and expressiveness.

As shown in Table VII, the proposed model was trained and tested on an NVIDIA GeForce RTX 3070 Ti with 8 GB of GDDR6 memory, enabling efficient acceleration of the deep learning processes. For real-world deployment, experiments utilized an NVIDIA Jetson Xavier NX, featuring a 6-core Carmel ARM v8.2 CPU and a Volta GPU with 48 Tensor Cores, providing up to 21 TOPS (INT8) of AI performance. Its configurable power consumption (10W/15W/20W) and 8GB LPDDR4x memory with 51.2 GB/s bandwidth support effective real-time inference at the edge with low latency.

V. RESULTS AND DISCUSSIONS

A. Performance on Closed-Set RFFI

Model training is conducted for each architecture with different preprocessing techniques on the SingleDay and ManyTx datasets. The loss and accuracy curves as a function of epochs for the model trained on the SingleDay and ManyTx datasets are shown in Figure 4 and Figure 5, respectively. The accuracy

TABLE VII
HARDWARE SPECIFICATIONS FOR TRAINING AND DEPLOYMENT

Property	GeForce RTX 3070Ti	Jetson Xavier NX
GPU	NVIDIA GeForce RTX 3070Ti	NVIDIA Volta
CPU	Core i7-8700K	Carmel Arm v8.2
RAM	64 GB	8 GB
Power usage	240 W	10 W / 15 W / 20 W
Purpose	Training and testing	Real-world deployment

and F1 metrics of the trained models on the test set are listed in Table I, while a comparison with baseline methods without preprocessing is provided in Table III.

The training dynamics of HyDRA (TDSE) and HyDRA (MLFE) on the SingleDay and ManyTx datasets show distinct trends. On SingleDay (Figure 4), both models converge rapidly, with losses stabilizing below 0.1 and accuracies nearing 100% by epoch 10. On the more challenging ManyTx dataset (Figure 5), convergence is slower. The effect of our ReduceLRonPlateau scheduler is particularly pronounced on ManyTx, where learning rate adjustments lead to significant loss reductions. For instance, around epoch 100 for TDSE and epoch 65 for MLFE, both models exhibit noticeable declines in validation loss, coinciding with learning rate reductions, which effectively mitigate overfitting and improve convergence on this more complex dataset. This scheduler’s impact is less pronounced on SingleDay, where the loss is already low due to the dataset’s simpler nature.

We observe that all combinations of model architecture and preprocessing techniques exhibit significantly higher performance on the SingleDay dataset than on ManyTx since the latter has more transmitters, fewer available signal segments for each transmitter (See Table II), and is collected on 4 different days. On SingleDay, our proposed HyDRA (TDSE), based on a CNN+Transformer architecture, achieves an accuracy of 99.78% without preprocessing, while HyDRA (MLFE), leveraging a CNN+Mamba architecture, reaches 99.67%, both delivering state-of-the-art (SOTA) performance that surpasses all baseline methods such as CNN-TFLite (99%) and CNN (85%). On ManyTx, HyDRA (TDSE) achieves a remarkable 90.22% accuracy and HyDRA (MLFE) reaches 89.34%, likewise attaining SOTA accuracy and outperforming all baselines including MobileNet MCRFF (86.4%) and WiSigNet (53.1%), with TDSE slightly ahead of MLFE. After adopting our proposed lossless VMD, HyDRA (TDSE) and HyDRA (MLFE) further improve to 99.81% and 99.71% on SingleDay, and 90.71% and 89.82% on ManyTx, respectively, demonstrating their effectiveness across both datasets.

B. Comparison between ADMM and lossless VMD

1) *Accuracy*: To validate the usefulness of the proposed lossless VMD preprocessing method, we controlled the mode number $k = 3$ and tested the model accuracy when either VMD (ADMM) or lossless VMD were applied to the TDSE and MLFE architecture. The raw TDSE/MLFE architecture with no preprocessing was set as the control group. It can be concluded from Table I that for all proposed model architectures, lossless VMD results in higher prediction accuracy

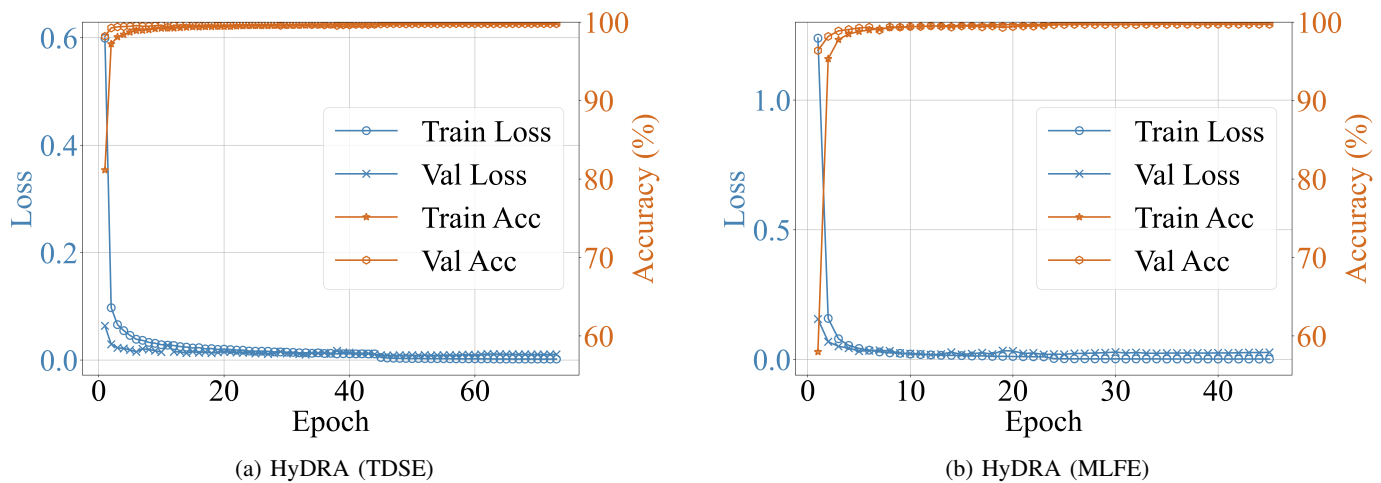


Fig. 4: The loss and accuracy curves as a function of epochs for the model trained on the SingleDay Dataset.

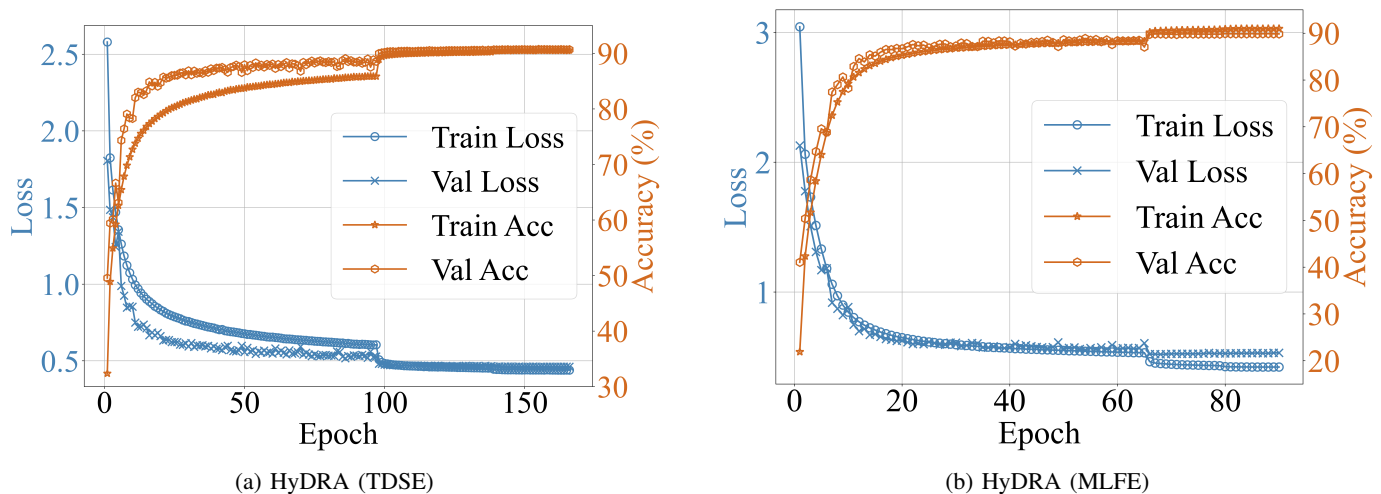


Fig. 5: The loss and accuracy curves as a function of epochs for the model trained on the ManyTx Dataset.

compared to the control group, especially in the ManyTx dataset with a 0.45% improvement. In comparison, VMD (ADMM) performs worse than the control group. This result can prove the claim in Section III. A that the information loss (specifically, loss of crucial spectral features of the transmitter and occasional failure in locating spectral peaks) caused by the nonzero reconstruction error term in the augmented Lagrangian of the ADMM algorithm impairs the model’s performance at high SNR scenarios. However, since the lossless VMD method does not introduce information loss, it can improve performance by helping the model recognize different frequency components of the input signal, especially in larger and more complex datasets.

2) *Execution Time*: To analyze the efficiency of the proposed lossless VMD preprocessing method, we compared the execution time of VMD with ADMM (penalty factor set as $\alpha = 2000$ proposed in the original paper [29]) and lossless VMD. Both methods were performed on 10% of the entries of the SingleDay dataset (22400 signal segments of length 256) on a Core i7-8700K CPU, and the average execution time was calculated for k between 2 and 7, shown in

Figure 6a. The figure indicates that VMD (ADMM) executes approximately exponentially long w.r.t. k , while the execution time of lossless VMD does not dramatically increase. When $k = 3$ (final choice of our model), the average execution time is 0.458ms for lossless VMD and 1.733ms, which is 73.6% faster than VMD (ADMM). The rate increases w.r.t k and reaches 95.9% (0.572ms versus 13.785ms) when $k = 7$, indicating that lossless VMD has a more significant advantage when decomposing into more IMF components. Since high execution time is unfavorable in real-world applications as it results in high latency, the low time cost is another advantage of lossless VMD.

C. *Effect of the Number of IMF Components*

To analyze the effect of IMF mode number k to the overall performance of the model, we trained the TDSE model on the ManyTx dataset preprocessed by lossless VMD with k from 1 to 7 ($k = 1$ is equivalent to raw IQ data with no preprocessing). Accuracy and F1 metrics are tested and sketched in Figure 6b.

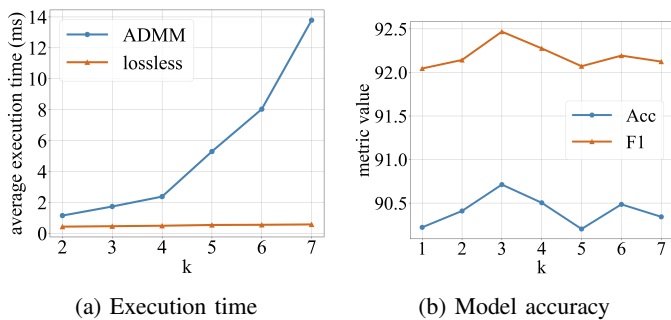


Fig. 6: Effect of different k values on the performance of the proposed model. Subfigure (a) compares the average execution time of ADMM and lossless VMD across varying k values. Subfigure (b) illustrates the influence of k on model accuracy and F1-score.

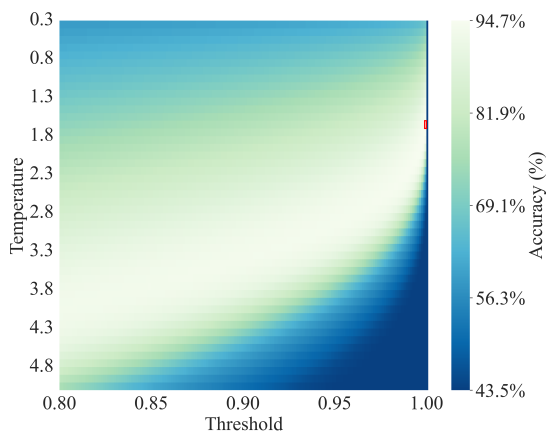


Fig. 7: Effect of different threshold and temperature values on Open-Set RFFI accuracy. The highest accuracy is highlighted with a red rectangle.

The figure indicates that both accuracy and F1 metrics increase and reach a peak of 90.71%/92.47% at $k = 3$, and then fall when k continues to increase. This result implies that small or moderate k helps the feature extraction of the CFRE layer, while large k may harm its ability to generalize. According to this experiment, we have chosen $k = 3$ as the final value for our model.

D. Comparison between HyDRA (TDSE) and HyDRA (MLFE)

Table VIII presents a comparison between HyDRA (TDSE) and HyDRA (MLFE), both trained and tested on the SingleDay dataset with lossless VMD preprocessing. HyDRA (TDSE) achieves an accuracy of 99.81%, slightly ahead of HyDRA (MLFE) at 99.71%, showcasing its strong precision on this dataset. In training time, MLFE stands out with 856.0 seconds, nearly 5.8 times faster than TDSE’s 4929.3 seconds, highlighting its clear efficiency advantage. For model size, MLFE’s 394 KB contrasts with TDSE’s 600 KB, emphasizing MLFE’s suitability for resource-efficient deployment. Both models maintain identical FLOPs of 15,746,816, ensuring consistent computational complexity. The parameter count shows TDSE at 146,876 and MLFE at 96,060, with MLFE’s

TABLE VIII
COMPARISON BETWEEN HYDRA (TDSE) AND HYDRA (MLFE)

Property	HyDRA (TDSE)	HyDRA (MLFE)
Accuracy	99.81%	99.71%
Training Time	4929.3s	856.0s
Model Size	600 KB	394 KB
FLOPs	15,746,816	15,746,816
Parameter Count	146,876	96,060
Inf. Time (GeForce RTX 3070Ti)	0.4219ms	0.3962ms
Inf. Time (Jetson Xavier NX)	8.4073ms	78.2622ms*

* Using Mamba-minimal instead of the official Mamba. This does not represent the best outcome.

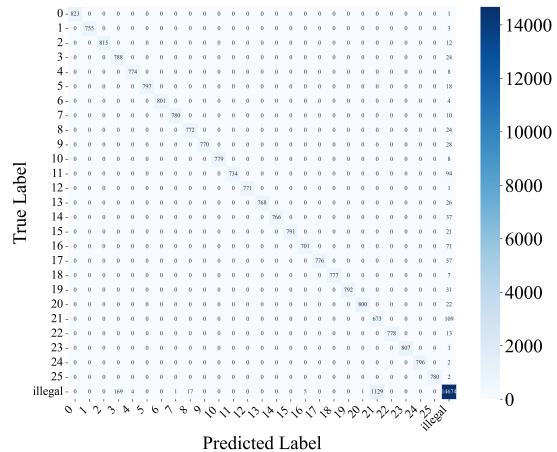


Fig. 8: The confusion matrix for Open-Set RFFI at Temperature 1.6 and Threshold 0.999.

streamlined design maintaining near-equivalent accuracy at a lower scale, further supporting its efficiency. On the GeForce RTX 3070Ti, MLFE delivers an inference time of 0.3962 ms, slightly faster than TDSE’s 0.4219 ms, reinforcing its speed benefit. These results highlight TDSE’s strength in high accuracy and MLFE’s advantages in training speed, model compactness, and inference efficiency.

E. Performance on Open-Set RFFI

Our algorithm employs the HyDRA (TDSE) model for open-set classification, trained on 26 legal transmitters from the SingleDay dataset, to distinguish legal from illegal devices while detecting unauthorized transmitters in real-world RFFI scenarios. The effect of different threshold and temperature values on open-set RFFI accuracy is illustrated in Figure 7, where the temperature ranges from 0.3 to 5.0 with a step size of 0.1, and the threshold ranges from 0.800 to 1.000 with a step size of 0.001. The highest accuracy, marked by a red rectangle, reaches 94.67% at a temperature of 1.6 and a threshold of 0.999. For thresholds below 1, a corresponding temperature range can always be found to achieve over 90% accuracy; however, at $\tau = 1$, the accuracy drops significantly to around 45%.

Generally, higher thresholds require lower temperatures to maintain high accuracy: as the threshold increases from 0.800 to 0.999, the optimal temperature decreases from approxi-

mately 4 to 2. The temperature parameter T governs the smoothness of the softmax probability distribution—a higher T results in a softer, more uniform distribution, whereas a lower T sharpens the probabilities. At higher thresholds, a lower temperature sharpens the distribution, ensuring high confidence in legal classifications and effective rejection of illegal devices, while setting $\tau = 1$ overly sharpens the probabilities, leading to excessive rejections. This trade-off between temperature and threshold is clarified by the temperature-scaled softmax formulation in eq. (20).

The confusion matrix at the optimal temperature of 1.6 and threshold of 0.999, shown in Figure 8, highlights the model’s performance. The model achieves high accuracy, correctly identifying most legal transmitters (0 to 25) along the diagonal and classifying a substantial number of illegal devices as illegal, demonstrating robustness in open-set scenarios. However, some illegal devices are misclassified as legal transmitters, notably as transmitter 21, indicating that certain illegal devices may have RF fingerprints similar to legal ones, which presents a challenge for accurate differentiation.

F. Edge Device Deployment

The HyDRA models, deployed on the NVIDIA Jetson Xavier NX edge computing platform (shown in Figure 9), demonstrate effective performance tailored to their respective configurations, as detailed in Table VIII. To address the incompatibility of the official Mamba library with the edge device’s PyTorch version, we propose a solution by substituting the Mamba core component in HyDRA (MLFE) with Mamba-minimal¹, a streamlined variant of Mamba. This substitution ensures input-output consistency but results in reduced runtime efficiency compared to the official Mamba implementation, which does not represent the optimal outcome. For a detailed assessment of the performance differences between Mamba-minimal and the official Mamba library, refer to the information provided in the Mamba-minimal GitHub repository. HyDRA (TDSE) achieves an inference time of 8.4073 ms, while HyDRA (MLFE) records an inference time of 78.2622 ms. The inference times reported in the table represent the average of 1000 runs following a 10-run warm-up phase. These results underscore the suitability of both models for edge device applications, with HyDRA (TDSE) offering rapid inference and HyDRA (MLFE) benefiting from a reduced parameter count, making them adaptable to diverse data processing needs in resource-constrained settings.

VI. CONCLUSION

This paper introduces HyDRA, a Hybrid Dual-mode RF Architecture that enhances Radio Frequency Fingerprint Identification (RFFI) by addressing challenges in dynamic and open-set environments. Unlike traditional methods, HyDRA integrates an optimized Variational Mode Decomposition (VMD) that boosts preprocessing efficiency and accuracy through fixed center frequencies and closed-form solutions. Its adaptable architecture, with a Transformer-based TDSE and

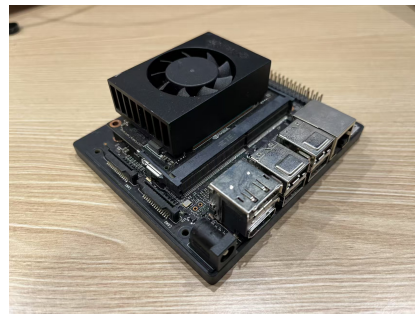


Fig. 9: NVIDIA Jetson Xavier NX

a Mamba-based MLFE, delivers robust performance across diverse conditions. Testing on public datasets confirms HyDRA’s exceptional closed-set accuracy and reliable open-set classification, effectively identifying unauthorized devices. Deployment on the NVIDIA Jetson Xavier NX further validates its practicality, achieving millisecond-level inference with low power consumption. Future work will focus on enabling HyDRA for real-time signal transmission and reception via antenna integration, processing and classifying incoming signals online, and determining their legitimacy without relying on preprocessed offline datasets, strengthening its potential for practical wireless security solutions. This will involve tackling challenges such as real-time signal synchronization, optimizing online VMD processing for low-latency performance, and developing adaptive thresholding for robust open-set classification, ultimately enhancing HyDRA’s applicability in real-time wireless security solutions.

ACKNOWLEDGMENTS

The authors express their sincere gratitude to Professor Danijela Cabric for her invaluable guidance, insightful suggestions, and continuous support throughout this research. We are particularly thankful for her generous provision of the WiSig dataset, which was instrumental in enhancing the quality and depth of our work.

APPENDIX A MATHEMATICAL DETAILS OF LOSSLESS VMD

Let $x_k(t)$ be the analytic, baseband version of $u_k(t)$, i.e.

$$x_k(t) = \partial_t \left[\left(\delta(t) + \frac{j}{\pi t} \right) * u_k(t) \right] e^{-j\omega_k t}$$

Perform Fourier transform on both sides.

$$\begin{aligned} X_k(\omega) &= \mathcal{F}\{x_k(t)\} \\ &= j\omega \cdot \{[1 + \text{sgn}(\omega)]U_k(\omega) * \delta(\omega + \omega_k)\} \\ &= j\omega[1 + \text{sgn}(\omega + \omega_k)]U_k(\omega + \omega_k) \end{aligned}$$

¹<https://github.com/johnma2006/mamba-minimal>

Using the Parseval's relation, the square of its L^2 norm is

$$\begin{aligned} \|x_k(t)\|_2^2 &= \int_{-\infty}^{+\infty} |x_k(t)|^2 dt = \int_{-\infty}^{+\infty} |X_k(\omega)|^2 d\omega \\ &= \int_{-\infty}^{+\infty} |j\omega[1 + \text{sgn}(\omega + \omega_k)]U_k(\omega + \omega_k)|^2 d\omega \\ &= \int_{-\infty}^{+\infty} |j(\omega - \omega_k)[1 + \text{sgn}(\omega)]U_k(\omega)|^2 d\omega \\ &= \int_0^{+\infty} 4(\omega - \omega_k)^2 |U_k(\omega)|^2 d\omega \end{aligned}$$

Plug it into eq. (1) we derive eq. (2).

When ω_k is fixed, we consider each $\omega \geq 0$ separately, since the integrated term does not depend on other frequency components. The optimization problem thus turns into

$$\begin{aligned} \arg \min_{\{U_k(\omega)\}} \left\{ \sum_k 4(\omega - \omega_k)^2 |U_k(\omega)|^2 \right\} \\ \text{s.t. } \sum_k U_k(\omega) = F(\omega) \end{aligned}$$

Let $\beta_k = 4(\omega - \omega_k)^2 \geq 0$, $\alpha_k = U_k(\omega)/F(\omega)$, we rewrite the problem as

$$\arg \min_{\{\alpha_k\}} \left\{ \sum_k \beta_k |\alpha_k|^2 \right\} \quad \text{s.t. } \sum_k \alpha_k = 1$$

It is evident that α_k must be real, or we can replace α_k with $Re(\alpha_k)$ to decrease $L(\alpha) = \sum_k \beta_k |\alpha_k|^2$.

Using the Cauchy-Schwartz inequality, we have

$$\sum_k \beta_k \alpha_k^2 \cdot \sum_k \beta_k^{-1} \geq \left(\sum_k \alpha_k \right)^2 = 1$$

and the equality holds when α_k/β_k is a constant, i.e., $\alpha_k \propto (\omega - \omega_k)^2$, which derives eq. (3). Plugging eq. (3) into eq. (2) gives eq. (4).

REFERENCES

- [1] D. Nouichi, M. Abdelsalam, Q. Nasir, and S. Abbas, "Iot devices security using rf fingerprinting," in *2019 Advances in Science and Engineering Technology International Conferences (ASET)*, 2019, pp. 1–7.
- [2] K. Merchant, S. Revay, G. Stantchev, and B. Noursain, "Deep learning for rf device fingerprinting in cognitive communication networks," *IEEE Journal of Selected Topics in Signal Processing*, vol. 12, no. 1, pp. 160–167, 2018.
- [3] G. Baldini, R. Giuliani, G. Steri, I. Sanchez, and C. Gentile, "The application of the symbolic aggregate approximation algorithm (sax) to radio frequency fingerprinting of iot devices," in *2017 IEEE Symposium on Communications and Vehicular Technology (SCVT)*, 2017, pp. 1–6.
- [4] Y. Liu, J. Wang, J. Li, H. Song, T. Yang, S. Niu, and Z. Ming, "Zero-bias deep learning for accurate identification of internet-of-things (iot) devices," *IEEE Internet of Things Journal*, vol. 8, no. 4, pp. 2627–2634, 2021.
- [5] T. Zhao, B. W. Domae, C. Steigerwald, L. B. Paradis, T. Chabuk, and D. Cabric, "Drone rf signal detection and fingerprinting: Uavsig dataset and deep learning approach," in *MILCOM 2024 - 2024 IEEE Military Communications Conference (MILCOM)*, 2024, pp. 431–436.
- [6] Q. Tian, J. Jia, and C. Hou, "Research on fingerprint identification of wireless devices based on information fusion," *Mobile Networks and Applications*, vol. 25, 2020.
- [7] A. Vaswani, N. Shazeer, N. Parmar, J. Uszkoreit, L. Jones, A. N. Gomez, L. Kaiser, and I. Polosukhin, "Attention is all you need," in *Proceedings of the 31st International Conference on Neural Information Processing Systems*, ser. NIPS'17. Red Hook, NY, USA: Curran Associates Inc., 2017, p. 6000–6010.
- [8] J. Liu, F. R. Yu, C.-H. Lung, and H. Tang, "Optimal combined intrusion detection and biometric-based continuous authentication in high security mobile ad hoc networks," *IEEE Transactions on Wireless Communications*, vol. 8, no. 2, pp. 806–815, 2009.
- [9] J. Zhang, F. Wang, O. A. Dobre, and Z. Zhong, "Specific emitter identification via hilbert–huang transform in single-hop and relaying scenarios," *IEEE Transactions on Information Forensics and Security*, vol. 11, no. 6, pp. 1192–1205, 2016.
- [10] Z. Caidan, W. Xiongpeng, H. Lianfen, Y. Yan, and C. Yao-Chung, "Compressed sensing based fingerprint identification for wireless transmitters," *Scientific World Journal*, 2014.
- [11] J. S. Smith, "The local mean decomposition and its application to eeg perception data," *Journal of The Royal Society Interface*, vol. 2, no. 5, pp. 443–454, 2005.
- [12] S. Ur Rehman, K. Sowerby, C. Coghill, and W. Holmes, "The analysis of rf fingerprinting for low-end wireless receivers with application to ieee 802.11a," in *2012 International Conference on Selected Topics in Mobile and Wireless Networking*, 2012, pp. 24–29.
- [13] G. Montavon, W. Samek, and K.-R. Müller, "Methods for interpreting and understanding deep neural networks," *Digital Signal Processing*, vol. 73, pp. 1–15, 2018.
- [14] D. Roy, T. Mukherjee, M. Chatterjee, E. Blasch, and E. Pasiliao, "Rfal: Adversarial learning for rf transmitter identification and classification," *IEEE Transactions on Cognitive Communications and Networking*, vol. 6, no. 2, pp. 783–801, 2020.
- [15] X. Wang, X. Wang, and S. Mao, "Rf sensing in the internet of things: A general deep learning framework," *IEEE Communications Magazine*, vol. 56, no. 9, pp. 62–67, 2018.
- [16] G. Qing, H. Wang, and T. Zhang, "Radio frequency fingerprinting identification for zigbee via lightweight cnn," *Physical Communication*, vol. 44, p. 101250, 2021.
- [17] L. Peng, J. Zhang, M. Liu, and A. Hu, "Deep learning based rf fingerprint identification using differential constellation trace figure," *IEEE Transactions on Vehicular Technology*, vol. 69, no. 1, pp. 1091–1095, 2020.
- [18] S. Taşcıoğlu, M. Köse, and Z. Telatar, "Effect of sampling rate on transient based rf fingerprinting," in *2017 10th International Conference on Electrical and Electronics Engineering (ELECO)*, 2017, pp. 1156–1160.
- [19] I. S. Mohamed, Y. Dalveren, and A. Kara, "Performance assessment of transient signal detection methods and superiority of energy criterion (ec) method," *IEEE Access*, vol. 8, pp. 115 613–115 620, 2020.
- [20] E. Uzundurukan, A. Ali, Y. Dalveren, and A. Kara, "Performance analysis of modular rf front end for rf fingerprinting of bluetooth devices," *Wireless Personal Communications*, vol. 112, 06 2020.
- [21] G. O. Zamora, S. Bergin, and I. O. Kennedy, "Using support vector machines for passive steady state rf fingerprinting," in *Novel Algorithms and Techniques in Telecommunications and Networking*, T. Sobh, K. Elleithy, and A. Mahmood, Eds. Dordrecht: Springer Netherlands, 2010, pp. 183–188.
- [22] C. Zhao, M. Huang, L. Huang, X. Du, and M. Guizani, "A robust authentication scheme based on physical-layer phase noise fingerprint for emerging wireless networks," *Computer Networks*, vol. 128, pp. 164–171, 2017, survivability Strategies for Emerging Wireless Networks.
- [23] T. Jian, B. C. Rendon, E. Ojuba, N. Soltani, Z. Wang, K. Sankhe, A. Gritsenko, J. Dy, K. Chowdhury, and S. Ioannidis, "Deep learning for rf fingerprinting: A massive experimental study," *IEEE Internet of Things Magazine*, vol. 3, no. 1, pp. 50–57, 2020.
- [24] B. Kim, Y. E. Sagduyu, K. Davaslioglu, T. Erpek, and S. Ulukus, "Channel-aware adversarial attacks against deep learning-based wireless signal classifiers," *IEEE Transactions on Wireless Communications*, vol. 21, no. 6, pp. 3868–3880, 2022.
- [25] J. Robinson, S. Kuzdeba, J. Stankowicz, and J. M. Carmack, "Dilated causal convolutional model for rf fingerprinting," in *2020 10th Annual Computing and Communication Workshop and Conference (CCWC)*, 2020, pp. 0157–0162.
- [26] C. Zhao, J. Yu, G. Luo, and Z. Wu, "Radio frequency fingerprinting identification of few-shot wireless signals based on deep metric learning," *Wireless Communications and Mobile Computing*, vol. 2023, no. 1, p. 2132148, 2023.
- [27] N. E. Huang, Z. Shen, S. R. Long, M. C. Wu, H. H. Shih, Q. Zheng, N.-C. Yen, C. C. Tung, and H. H. Liu, "The empirical mode decomposition and the hilbert spectrum for nonlinear and non-stationary time series analysis," *Proceedings of the Royal Society of London. Series A: Mathematical, Physical and Engineering Sciences*, vol. 454, no. 1971,

- pp. 903–995, 1998.
- [28] J. Flamant, N. Le Bihan, and P. Chainais, “Time–frequency analysis of bivariate signals,” *Applied and Computational Harmonic Analysis*, vol. 46, no. 2, pp. 351–383, 2019.
 - [29] K. Dragomiretskiy and D. Zosso, “Variational mode decomposition,” *IEEE Transactions on Signal Processing*, vol. 62, no. 3, pp. 531–544, 2014.
 - [30] R. Xie, W. Xu, Y. Chen, J. Yu, A. Hu, D. W. K. Ng, and A. L. Swindlehurst, “A generalizable model-and-data driven approach for open-set rff authentication,” *IEEE Transactions on Information Forensics and Security*, vol. 16, pp. 4435–4450, 2021.
 - [31] S. Hanna, S. Karunaratne, and D. Cabric, “Wisig: A large-scale wifi signal dataset for receiver and channel agnostic rf fingerprinting,” *IEEE Access*, vol. 10, pp. 22 808–22 818, 2022.
 - [32] F. zhuo, Y. Huang, and J. chen, “Radio frequency fingerprint extraction of radio emitter based on i/q imbalance,” *Procedia Computer Science*, vol. 107, pp. 472–477, 2017, advances in Information and Communication Technology: Proceedings of 7th International Congress of Information and Communication Technology (ICICT2017).
 - [33] J. Wang, C. Zhan, S. Li, Q. Zhao, J. Liu, and Z. Xie, “Adaptive variational mode decomposition based on archimedes optimization algorithm and its application to bearing fault diagnosis,” *Measurement*, vol. 191, p. 110798, 2022.
 - [34] H. Jia, Y. Zhiyong, and Y. Jian, “Real-world uav recognition based on radio frequency fingerprinting with transformer,” *IET Communications*, vol. 19, 2025.
 - [35] K. Merchant and B. Nousain, “Enhanced rf fingerprinting for iot devices with recurrent neural networks,” in *MILCOM 2019 - 2019 IEEE Military Communications Conference (MILCOM)*, 2019, pp. 590–597.
 - [36] S. Al-Hazbi, A. Hussain, S. Sciancalepore, G. Oligeri, and P. Papadimitratos, “Radio frequency fingerprinting via deep learning: Challenges and opportunities,” in *2024 International Wireless Communications and Mobile Computing (IWCMC)*, 2024, pp. 0824–0829.
 - [37] J. Feng, X. Tang, B. Zhang, and Y. Ren, “Lightweight cnn-based rf fingerprint recognition method,” in *2023 8th International Conference on Computer and Communication Systems (ICCCS)*, 2023, pp. 1031–1035.
 - [38] A. M. Hussain, N. Abughanam, and P. Papadimitratos, “Edge ai-based radio frequency fingerprinting for iot networks,” *IEEE Internet of Things Journal*, vol. 10, no. 12, pp. 10 545–10 556, 2023.
 - [39] C. Sun, X. Chen, W. Wang, and H. Yin, “A transformer-based multi-feature extraction neural network for bluetooth devices identification,” in *2023 9th International Conference on Computer and Communications (ICCC)*, 2023, pp. 1469–1473.
 - [40] M. Zhan, Y. Li, H. Cui, B. Li, J. Zhang, C. Li, and W. Wang, “Mcrff: A meta-contrastive learning-based rf fingerprinting method,” in *MILCOM 2023 - 2023 IEEE Military Communications Conference (MILCOM)*, 2023, pp. 391–396.
 - [41] M. Sandler, A. Howard, M. Zhu, A. Zhmoginov, and L.-C. Chen, “Mobilenetv2: Inverted residuals and linear bottlenecks,” in *Proceedings of the IEEE Conference on Computer Vision and Pattern Recognition (CVPR)*, June 2018.